# General synthesis of high-entropy alloy and ceramic nanoparticles in nanoseconds

**Zhigang Zou** ( zgzou@nju.edu.cn )
Nanjing University
**Bing Wang**
Nanjing University
**Cheng Wang**
Nanjing University
**Xiwen Yu**
Nanjing University
**Yuan Cao**
Nanjing Univeristy
**Linfeng Gao**
Nanjing University
**Wenjun Luo**
Nanjing University https://orcid.org/0000-0001-6760-6929
**Congping Wu**
Nanjing University
**Yingfang Yao**
Nanjing University
**Zhiqun Lin**
Georgia Institute of Technology https://orcid.org/0000-0003-3158-9340

**Physical Sciences - Article**

**Keywords:** High-entropy materials (HEMs), high-entropy alloys (HEAs), laser scanning ablation (LSA)

**Posted Date:** December 28th, 2020

**DOI:** https://doi.org/10.21203/rs.3.rs-116889/v1

**Version of Record:** A version of this preprint was published at Nature Synthesis on February 10th, 2022. See the published version at https://doi.org/10.1038/s44160-021-00004-1.

# General synthesis of high-entropy alloy and ceramic nanoparticles in nanoseconds

**Authors:** Bing Wang[1,2,4,7], Cheng Wang[3], Xiwen Yu[3], Yuan Cao[1], Linfeng Gao[3], Wenjun Luo [1,3,4,7], Congping Wu[1,7], Yingfang Yao[1,3,4,7] ✉, Zhiqun Lin[2]✉, Zhigang Zou[1,3,4,5,6,7]✉.

**Affiliations:**

[1]Eco-materials and Renewable Energy Research Center (ERERC), School of Physics, Nanjing University, No. 22 Hankou Road, Nanjing 210093, P. R. China.

[2]School of Materials Science and Engineering, Georgia Institute of Technology, Atlanta GA 30332, USA.

[3]College of Engineering and Applied Sciences, Nanjing University, No. 22 Hankou Road, Nanjing 210093, P. R. China.

[4]Jiangsu Key Laboratory for Nano Technology, National Laboratory of Solid State Microstructures, Nanjing University, No. 22 Hankou Road, Nanjing 210093, P. R. China.

[5]School of Science and Engineering, The Chinese University of Hong Kong, Shenzhen, 2001 Longxiang Blvd., Longgang District, Shenzhen, 518172, P. R. China.

[6]Macau Institute of Systems Engineering, Macau University of Science and Technology, Macau 999078, China.

[7]Kunshan Innovation Institute of Nanjing University, 1699 Zuchongzhi South Road, Kunshan, Jiangsu 215347, P. R. China.

✉Correspondence to: zgzou@nju.edu.cn (Z. Z.); zhiqun.lin@mse.gatech.edu (Z. L.); yaoyingfang@nju.edu.cn (Y. Y.).

**Abstract: High-entropy materials (HEMs) including high-entropy alloys (HEAs) and high-entropy ceramics (HECs) at nanoscale have promising prospects in many fields, yet a robust synthesis strategy is lacking. Herein, we present a simple and general approach, laser scanning ablation (LSA), to synthesize a vast library of HEA and HEC nanoparticles (NPs) including alloys, sulfides, oxides, borides, nitrides, phosphides. The LSA method takes only 5 nanoseconds per pulse to ablate the corresponding NPs precursors at atmospheric temperature and pressure in alkanes. The ultra-rapid process ensures up to 9 dissimilar metallic elements combined uniformly regardless of their thermodynamic solubility. As laser pulse precisely confines energy to desired microregions, the LSA method enables HEM NPs loading on various substrates, even thermally-sensitive ones such as metals and glass. Applied as electrocatalysts for overall water splitting, HEM NPs achieved an overpotential of 185 mV @ 10mA $cm^{-2}$, which was among the best activities. The LSA technique discloses a large collection of new nanostructured HEMs with unique properties and attractive functions. We believe this general strategy will provide a versatile and flexible material platform for a wild range of fields such as biology, catalysis, electronics and magnetics.**

High-entropy materials (HEMs), including high-entropy alloys (HEAs) and high-entropy ceramics (HECs), are a class of materials that contain at least five near-equimolar principal metal atoms in an amorphous structure or a solid-solution phase[1,2]. These unconventional compositions and structures offer HEMs unprecedented physicochemical properties such as high strength[3], unique electrical and magnetic properties[4], and promising resistances to wear, oxidation and corrosion[5]. However, it is still a daunting task of integrating multiple elements into HEMs at nanoscale which can open up an effective avenue to tune their properties for vast applications.

A few synthesis techniques including carbothermal shock[6], moving bed pyrolysis[7], ultrasonication-assisted wet chemistry method[8], laser-assisted strategy[9] and electrosynthesis[10] have been reported for HEA nanoparticles (NPs) synthesis. However, current methods generally require rigorous conditions including high pressure, temperature and inert atmospheric protection. [6-8] They often produce NPs immobilized on limited thermally-resistant substrates rather than thermally-sensitive ones. On the other hand, despite some synthesis methods under mild conditions,[9,10] they either require targets with the same composition as the NPs, or can only craft amorphous NPs, which narrows the varieties of HEA NPs. Surprisingly, strategies for the creation of HEC NPs have not yet been explored because research on HEC materials is still in its infancy since its birth in 2015[11]. Clearly, it is of great significance to develop a general yet robust route to synthesize both HEA and HEC NPs under mild conditions over a diversity of substrates.

Herein, we exploited a laser scanning ablation (LSA) approach using pulsed fiber nanosecond laser to synthesize a library of HEA and HEC NPs at atmospheric temperature and pressure. The laser ablates the corresponding NPs precursors in alkanes, enabling the formation of HEA and HEC (i.e. oxide, sulfide, phosphide, nitride and boride) NPs within only a 5-nanosecond (ns) pulse. The ultra-rapid process ensures up to 9 metallic elements to combine uniformly regardless of their thermodynamic solubility. As the laser pulse precisely confine energy to desired microregions, HEM NPs can form on various substrates, even thermally-sensitive ones such as metals and glass. To prove utility, HEM NPs loaded on graphene was integrated as both the anode and cathode for electrochemically overall water splitting. It delivered 10 mA $cm^{-2}$ within only 1.42 V, far surpassing the performance of current catalysts. Our work develops a general and robust approach of both HEA and HEC NPs synthesis, and discloses a vast collection of new nanomaterials with unique properties and attractive functions.

**HEA NPs on carbon substrates**

In a typical LSA process, metal chlorides of equal molar ratio were firstly loaded onto a substrate. Then, the substrate was transferred to hexane, and irradiated by laser pulses at room temperature (R. T., ~25 $^{o}$C), as shown in Figs. 1a,1b and Supplementary Information section S1. At a constant average power density of $2\times10^5$ W/$cm^2$, a peak pulse power density of $2\times10^9$ W/$cm^2$ (Fig. 1c), calculated by pulse energy/pulse width, was used with the short pulse width of 5 nm for rapid HEM NP fabrication. As carbon nanofibers (CNFs) with surface-bound residual oxygen facilitated the melt metal movement and fission events[6], we first used CNFs

as the substrate (see Extended Data Fig. 1a) to support HEA NPs with Au, Fe, Co, Cu, Cr elements. As shown in Fig. 1d, HEA products are crafted efficiently on CNFs with uniform dispersion. Energy-dispersive X-ray spectroscopy (EDS) maps depict homogeneous distributions of all the five elements throughout the NP. Based on the atomic ratios (see Extended Data Fig. 1b), the configurational entropy ($\Delta S_{mix}$) of the AuFeCoCuCr NPs is calculated to be 13.3 J/mol·K, which is classified as HEA (see Supplementary Information section S2). Cl element mainly distributes on the NPs surface, indicating Cl was excluded during the formation of the HEA NPs. The residue chlorine can be completely removed by washing the NPs in ethanol to obtain highly-purified HEAs. Besides hexane, LSA is also successfully applied in other alkanes such as octane, decane and dodecane (see Extended Data Fig. 1c), indicating a broad liquid phase applicability of the LSA strategy.

We mainly used a model of photothermal evaporation to understand the formation mechanism of HEA NPs (see Supplementary Information section S3). The HEAs synthesis by the LSA entails a number of physicochemical processes (Fig. 2a)[12]. The incoming laser pulse penetrates through the alkane onto the substrate surface loaded with precursors (panel I). Due to the intense optical field and high transient temperature in the focus, the precursors are prone to melt or decompose after being irradiated. A high-temperature and high-pressure plume which composes of ions, atoms, clusters and vapors forms at the substrate/liquid interface (panel II), leading to a multielement mixture with the formation of solid solution phases due to the large $T\Delta S_{mix}$. Recoil from the plume generates emission shockwaves[13] which causes subsequent ultrasonic expansion of the plume into surrounding liquid (panel III). The plume

quickly cools down and releases energy to alkane (panel III), resulting in the HEA nucleation and coalescence (panel IV). Meanwhile, the energy release induces the generation of high-pressure and high-temperature bubbles expanding into the liquid (See Movie S1). During the expansion, the temperature and pressure inside the cavitation bubble reduce rapidly and recover to the original value once the bubble collapses (panel V). The high energy is consequently released with the formation of the HEA NPs. As the subsequent cooling down period is rapid driven by the ultrafast heat exchange between the ablated area and the surrounding liquid phase, the solid solution phase maintains without the formation of intermetallic phases. In this regime, despite different properties (e.g. atomic radius, electronegativity, reduction potentials) of metallic elements (see Supplementary Information section S4), a nanosecond metal reduction and alloying process in LSA allows the synthesis of HEA NPs with thermodynamically forbidden compositions and uniform elemental distributions. In the case of AuFeCoCuCr HEA NPs (Fig. 1d), the $\Delta S_{mix}$ of Au, Fe, Co, Cu, Cr atoms increased from 0 to 13.3 J/ mol·K after LSA (Fig. 2b). The LSA method also allows us to readily synthesize more complex HEA NPs including elements of Pt, Au, Pd, Cu, Cr, Sn, Fe, Co, Ni (Fig. 2c, 2d and Extended Data Fig. 2) with the calculated $\Delta S_{mix}$ of 17.4 J/ mol·K. The STEM elemental maps show uniform elemental distribution of Pt, Au, Pd, Cu, Cr, Sn, Fe, Co, Ni at an atomic scale. The High-Angle Annular Dark Field Scanning Transmission Electron micrograph (HAADF-STEM) and X-Ray Diffractometer (XRD) patterns confirm the FCC solid-solution phase structure of the novenary HEA-NPs.

To control the size and compositional distribution of HEA NPs, we proposed the strategies of changing the laser scanning times (see Extended Data Fig. 3, a more detailed discussion can be found in the Supplementary Information section S5) and adjusting the ablation temperature (see Extended Data Fig. 4). More uniform and smaller NPs indicated improved compositional distribution due to reduced metal loss caused by the lower temperature and pressure in the cavitation bubbles (see Supplementary Information section S5).

**HEA NPs on substrates other than carbon**

Besides CNFs, we also tried a series of carbon substrates such as graphene (see Extended Data Fig. 5a), carbon nanotubes (see Extended Data Fig. 5b), and even carbonized wood (see Extended Data Fig. 5c). HEA particles with size from nano- to micrometers have been loaded uniformly on these substrates with a high yield and great quality, revealing that LSA is an effective strategy for large-scale nano-/micro-manufacturing of HEAs onto any carbon substrates.

As laser pulse can precisely confine energy to desired microregions without altering the bulk properties of substrates[14], we then used LSA method to craft HEAs on substrates other than carbon, such as copper foam (see Extended Data Fig. 6a) and glass (see Extended Data Fig. 6b). HEAs form on the surfaces of these substrates, and each element is evenly distributed in the particles, demonstrating broad substrate applicability of LSA.

Notably, the size of HEA NPs under one laser pulse of the same power density is distinct when they are deposited onto different substrates (~11 nm for CNFs in Extended Data

Fig. 3b, ~700 nm for copper foam in Extended Data Fig. 6a). The distinction of particle sizes should be mainly caused by different thermal diffusion length of substrates, which can be interpreted by the following equation: $L_T=\sqrt{D\tau}$,[15,16] where D is the thermal diffusivity of the material and $\tau$ is the temporal pulse width of laser. During the HEA solidification process (Panel III and IV in Fig. 2a), the plume goes through a transient melting phase before the formation of HEA. The melting phase flows along the substrate surface from the hot central region to the rear cool regions (Marangoni effect[17]) to form melting pools[18]. This process is directly influenced by the thermal diffusion length of substrates. Carbon materials (i.e. graphene, nanotube and CNFs) have small thermal diffusivity ($0.1\sim7.6\times10^{-6}$ $m^2/s$)[19-21], with small thermal diffusion length (22~195 nm). In such a case, all of the optical energy is absorbed at the surface without significant thermal diffusion (see Extended Data Fig. 6c). In comparison, copper substrate has larger thermal diffusivity ($\sim1\times10^{-4}$ $m^2/s$) and thermal diffusion length (~710 nm)[22]. Higher thermal diffusion length leads to larger area of melting pools. As a result, larger HEA NPs with more melting pool marks were found on the surface of copper foam (see Extended Data Fig. 6a) due to a larger melting pool. For glass substrate, a large portion of the laser beam transmit through the transparent surface (see Extended Data Fig. 6c), and have no further interaction with the metal precursors. Thus, a few HEA NPs create on glass surface.

**Synthesis of HEC NPs**

As LSA method is a nonequilibrium route (rapid heating and cooling) which can decrease kinetic barriers to synthesize HEMs, we tried to apply LSA to synthesize HECs such

159 as high entropy sulfide (HES) and high entropy oxide (HEO). For HES precursor preparation,
160 we immersed the metal chlorides-loaded substrates into sulfur powder dissolved $CS_2$ (Fig. 3a).
161 Sulfur evenly deposited on CNFs after $CS_2$ fully volatized (see Extended Data Fig. 7a). For
162 HEO, the substrates with metal chlorides were treated by NaOH to form hydroxides as the
163 precursors (see Extended Data Fig. 7a). After LSA, the TEM images and the EDS maps
164 demonstrate the homogeneity of sulfur and oxygen elements in the HES (Fig. 3b) and HEO
165 NPs (Fig. 3c), respectively. The compositions of the HECs are uniform and no segregations
166 are detected. In order to exclude the possibility that the oxygen atoms generated during the
167 subsequent exposure of the sample to air, we exposed samples without NaOH treatment under
168 laser pulse. Oxygen was excluded from the CuCrFeCoNi HEA NPs (Extended Data Fig. 7b),
169 indicating oxygen atoms in metal hydroxides participated in the formation of HEO NPs during
170 the LSA process. When CNFs are replaced with graphene, HES and HEO particles can still be
171 produced by LSA method, as shown in Extended Data Fig. 7c, d. Both the XRD patterns of
172 HEOs and HESs with road diffraction hills and the selected area electron diffraction (SAED)
173 patterns with diffused halo rings implied their amorphous phases (see Extended Data Fig. 7e).
174 The UV-vis absorption of graphene with HEC NPs (see Extended Data Fig. 7f) decreased
175 compared with that of pristine graphene due to the light reflection or scattering on NPs. To
176 prove generality, we also successfully created other HECs such as high-entropy borides (Fig.
177 3d and Extended Data Fig. 8a), phosphides (Fig. 3e and Extended Data Fig. 8b), nitrides (Fig.
178 3f and Extended Data Fig. 8c) by LSA method, all of which showed amorphous phases
179 (Extended Data Fig. 8d).

The effects of lattice distortions, high mixing entropy and sluggish diffusion contribute to the formation of amorphous structures of HECs. The incorporation of nonmetallic atoms, such as sulfur, oxygen, phosphide, borides and nitrogen, reduces the growth rate of crystallites and expands the atomic space, leading to severe lattice distortion. The large lattice distortion causes high strain energy and thus raises the overall free energy[23]. In this case, amorphous structure with less coordination easily forms to relax the lattice distortion[24]. High entropy effect enhances complete mutual solubility of different atoms in the glassy structure of HECs, whereas the sluggish diffusion effect gives rise to the difficulty of atom mobility to form viable crystal structure[25]. Both effects play synergistic roles in the formation of amorphous structures of HECs. In addition, the rapid cooling rate during LSA process provides insufficient time and energy for crystallization, which is also a vitally important factor in their amorphization.

**Electrocatalytic Water splitting**

We demonstrated HEM NPs loaded on graphene as catalysts for electrocatalytic water splitting to generate $H_2$ and $O_2$. Pt/C and Ir/C have been widely used as commercial catalysts for hydrogen evaluation reaction (HER) and oxygen evaluation reaction (OER). However, the high cost of noble metals obstructs their popularization. HEAs are expected to decrease the loading of noble metals without losing their electrocatalytic efficiencies as noble metals can be highly dispersed in the HEA catalysts. In this work, we chose the low-amount noble metal HEAs of PtIrCuNiCr and PtAuPdFeNi as the catalysts for OER and HER reactions (Fig. 4a, Extended Data Fig. 9a, b). Fe, Ni are electron-rich atoms with both paired and unpaired d

electrons, while Cu and Cr are atoms with all the d orbitals of full and half-empty, respectively (Extended Data Fig. 9c). Based on the Brewer-Engel valence bond theory[26], electrocatalysts with both d electron pairs and half-empty d orbitals can improve electron transfer. As shown in Fig. 4b, the OER requires an overpotential of only 176 mV for PtIrCuCrNi and 178 mV for PtAuPdFeNi to deliver 10 mA $cm^{-2}$, which is much less than the state-of-the art Ir/C catalyst (248 mV) as well as the Ni foam (347 mV). For HER (Fig. 4c), the PtIrCuNiCr catalyst obtains -10 mA $cm^{-2}$ at an extremely low overpotential of 38 mV, which is lower than that of the Pt/C catalyst. Given the outstanding OER and HER activities of the PtIrCuCrNi NPs, we further utilized it as a bifunctional electrocatalyst for overall water splitting (Extended Data Fig. 9d). Remarkably, a current density of 10 mA $cm^{-2}$ was delivered at a combined overpotential of about 185 mV for electrochemical overall water splitting, which is superior to most previously reported bifunctional electrocatalysts (Fig. 4d and Supplementary Information section S6). The HEM electrode presented an excellent durability with no noticeable potential augment for more than 72 h of oxygen release at 200 mA $cm^{-2}$ (Fig. 4e), revealing the outstanding stability of the HEA catalyst for overall water splitting.

## Conclusions

We present a simple, general and scalable LSA route to create HEA and HEC NPs under mild conditions with broad substrate applicability. Through this method, the HEM nanostructure library is substantially advanced towards higher compositional diversity and structural complexity. By carefully designing HEM morphologies and screening their

components, HEM NPs will have promising prospect in a wide range of fields, such as biology, catalysis, electronics and magnetics.

## References


1 Ding, Q. Q. *et al.* Tuning element distribution, structure and properties by composition in high-entropy alloys. *Nature* **574**, 223-+, doi:10.1038/s41586-019-1617-1 (2019).

2 Oses, C., Toher, C. & Curtarolo, S. High-entropy ceramics. *Nat Rev Mater* **5**, 295-309, doi:10.1038/s41578-019-0170-8 (2020).

3 Li, Z. M., Pradeep, K. G., Deng, Y., Raabe, D. & Tasan, C. C. Metastable high-entropy dual-phase alloys overcome the strength-ductility trade-off. *Nature* **534**, 227-+, doi:10.1038/nature17981 (2016).

4 Berardan, D., Franger, S., Dragoe, D., Meena, A. K. & Dragoe, N. Colossal dielectric constant in high entropy oxides. *Phys Status Solidi-R* **10**, 328-333, doi:10.1002/pssr.201600043 (2016).

5 Sarkar, A. *et al.* High entropy oxides for reversible energy storage. *Nat Commun* **9**, doi:10.1038/s41467-018-05774-5 (2018).

6 Yao, Y. G. *et al.* Carbothermal shock synthesis of high-entropy-alloy nanoparticles. *Science* **359**, 1489-1494, doi:10.1126/science.aan5412 (2018).

7 Gao, S. J. *et al.* Synthesis of high-entropy alloy nanoparticles on supports by the fast moving bed pyrolysis. *Nat Commun* **11**, doi:10.1038/s41467-020-15934-1 (2020).

8 Liu, M. M. *et al.* Entropy-maximized synthesis of multimetallic nanoparticle catalysts via a ultrasonication-assisted wet chemistry method under ambient conditions. *Adv Mater Interfaces* **6**, 1900015, doi:10.1002/admi.201900015 (2019).

9 Waag, F. *et al.* Kinetically-controlled laser-synthesis of colloidal high-entropy alloy nanoparticles. *Rsc Adv* **9**, 18547-18558, doi:10.1039/c9ra03254a (2019).

10 Glasscott, M. W. *et al.* Electrosynthesis of high-entropy metallic glass nanoparticles for designer, multi-functional electrocatalysis. *Nat Commun* **10**, 2650, doi:10.1038/s41467-019-10303-z (2019).

11 Rost, C. M. *et al.* Entropy-stabilized oxides. *Nat Commun* **6**, doi:10.1038/ncomms9485 (2015).

12 Palneedi, H. *et al.* Laser irradiation of metal oxide films and nanostructures: applications and advances. *Adv Mater* **30**, doi:10.1002/adma.201705148 (2018).

13 Jeon, J. W. *et al.* The effect of laser pulse widths on laser-Ag nanoparticle interaction: Femto- to nanosecond lasers. *Appl Sci-Basel* **8**, doi:10.3390/app8010112 (2018).

14 Bewley, W. W. *et al.* Broad-stripe midinfrared photonic-crystal distributed-feedback lasers with laser-ablation confinement. *Appl Phys Lett* **83**, 5383-5385, doi:10.1063/1.1637153 (2003).

15 Miller, J. E., McDaniel, A. H. & Allendorf, M. D. Considerations in the design of materials for solar-driven fuel production using metal-oxide thermochemical cycles.

*Adv Energy Mater* **4**, doi:10.1002/aenm.201300469 (2014).
16 Ruffino, F. & Grimaldi, M. G. Nanostructuration of thin metal films by pulsed laser irradiations: A review. *Nanomaterials-Basel* **9**, doi:10.3390/nano9081133 (2019).
17 Bennett, T. D., Krajnovich, D. J., Grigoropoulos, C. P., Baumgart, P. & Tam, A. C. Marangoni mechanism in pulsed laser texturing of magnetic disk substrates. *J Heat Trans-T Asme* **119**, 589-596, doi:10.1115/1.2824146 (1997).
18 Semak, V. V., Knorovsky, G. A., MacCallum, D. O. & Roach, R. A. Effect of surface tension on melt pool dynamics during laser pulse interaction. *J Phys D Appl Phys* **39**, 590-595, doi:10.1088/0022-3727/39/3/025 (2006).
19 Vales-Pinzon, C. *et al.* Increasing the thermal conductivity of silicone based fluids using carbon nanofibers. *J Appl Phys* **120**, doi:10.1063/1.4969043 (2016).
20 Yue, Y. A., Huang, X. P. & Wang, X. W. Thermal transport in multiwall carbon nanotube buckypapers. *Phys Lett A* **374**, 4144-4151, doi:10.1016/j.physleta.2010.08.034 (2010).
21 Han, M., Xie, Y. S., Liu, J., Zhang, J. C. & Wang, X. W. Significantly reduced c-axis thermal diffusivity of graphene-based papers. *Nanotechnology* **29**, doi:10.1088/1361-6528/aabbc9 (2018).
22 Wood, R. F., Leboeuf, J. N., Chen, K. R., Geohegan, D. B. & Puretzky, A. A. Dynamics of plume propagation, splitting, and nanoparticle formation during pulsed-laser ablation. *Appl Surf Sci* **127**, 151-158, doi:10.1016/S0169-4332(97)00625-9 (1998).
23 He, Q. F. & Yang, Y. On lattice distortion in high entropy alloys. *Front Mater* **5**, doi:10.3389/fmats.2018.00042 (2018).
24 Tsai, C. W. *et al.* Strong amorphization of high-entropy AlBCrSiTi nitride film. *Thin Solid Films* **520**, 2613-2618, doi:10.1016/j.tsf.2011.11.025 (2012).
25 Inoue, A. High-strength bulk amorphous-alloys with low critical cooling rates. *Mater T Jim* **36**, 866-875, doi:10.2320/matertrans1989.36.866 (1995).
26 Molnar, A., Smith, G. V. & Bartok, M. New catalytic materials from amorphous metal-alloys. *Adv Catal* **36**, 329-383, doi:10.1016/S0360-0564(08)60020-6 (1989).

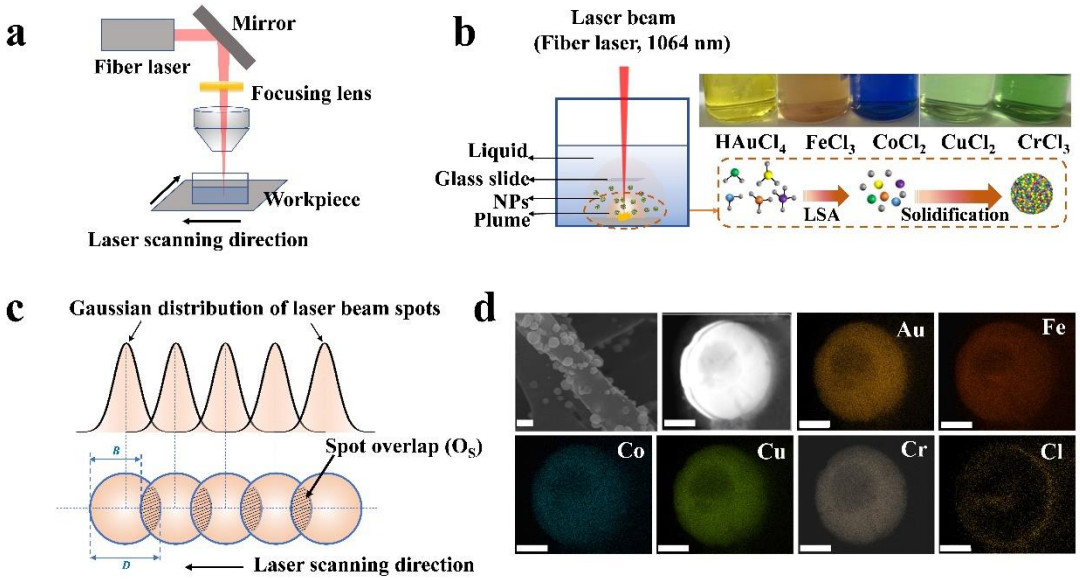


287

288 **Fig. 1. LSA synthesis of HEA NPs.** The schematic diagram of **a,** experimental set-up and **b,**

289 reaction process for synthesizing AuFeCoCuCr HEA NPs by the LSA method. **c,** The energy

290 distribution of a Gaussian laser beam with the power density of $2\times10^9$ W/cm$^2$ for the pulsed

291 fiber nanosecond laser. **d,** An SEM image of AuFeCoCuCr HEA NPs loaded on CNFs with

292 the scale bar of 100 nm; a TEM image of a AuFeCoCuCr HEA NP with the scale bar of 20 nm

293 and the corresponding EDS maps of Au, Fe, Co, Cu, Cr, Cl elements.

294

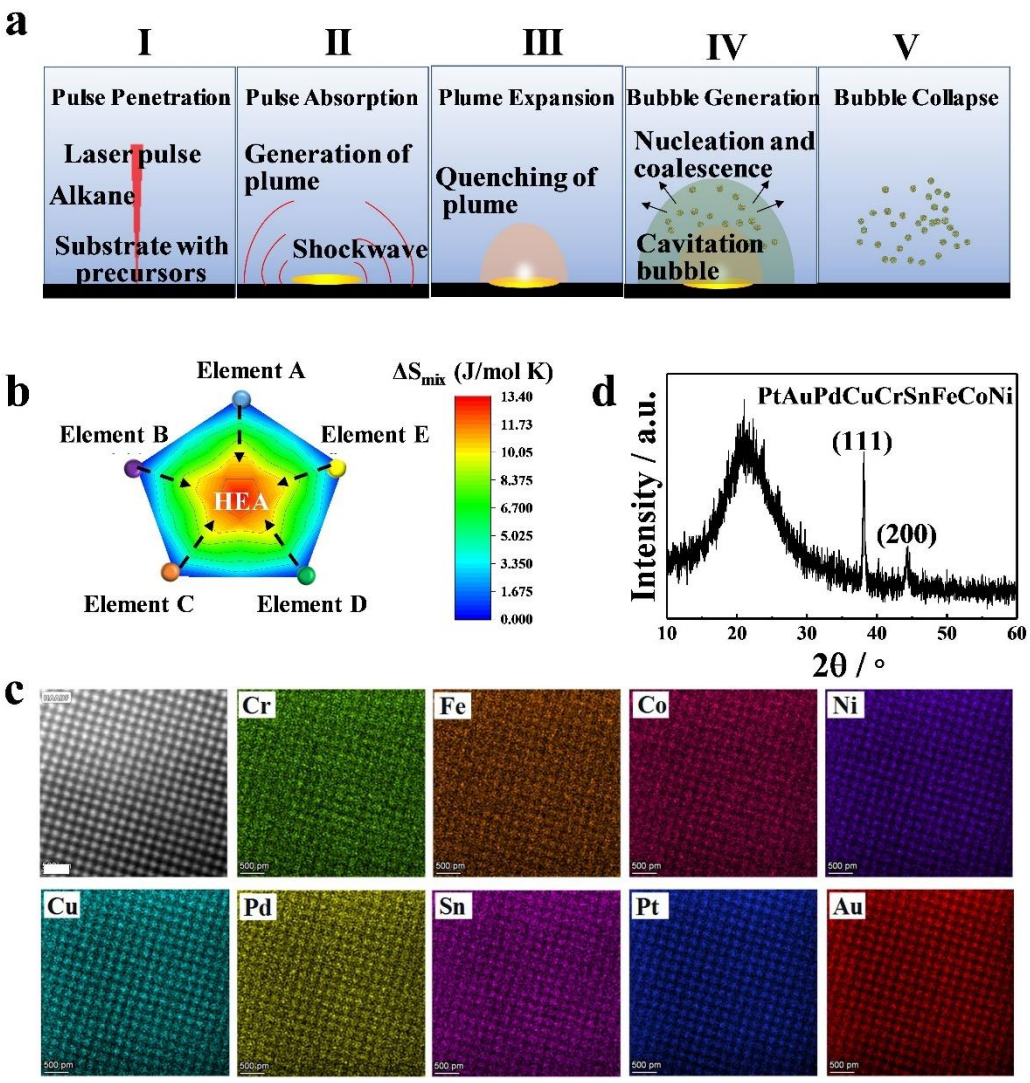


**Fig. 2. Formation mechanisms of HEA NPs for the LSA strategy. a,** Schematic illustration of formation mechanism of HEA NPs by LSA method. **b,** The configurational entropy evolution of HEAs with five elements during LSA process. **c,** Comparison of the local concentration distribution of individual elements for the same region. Atomic-scale HAADF-STEM images and STEM elemental maps for a novenary HEA NP (PtAuPdCuCrSnFeCoNi). **d,** XRD pattern of the novenary HEA-NPs.

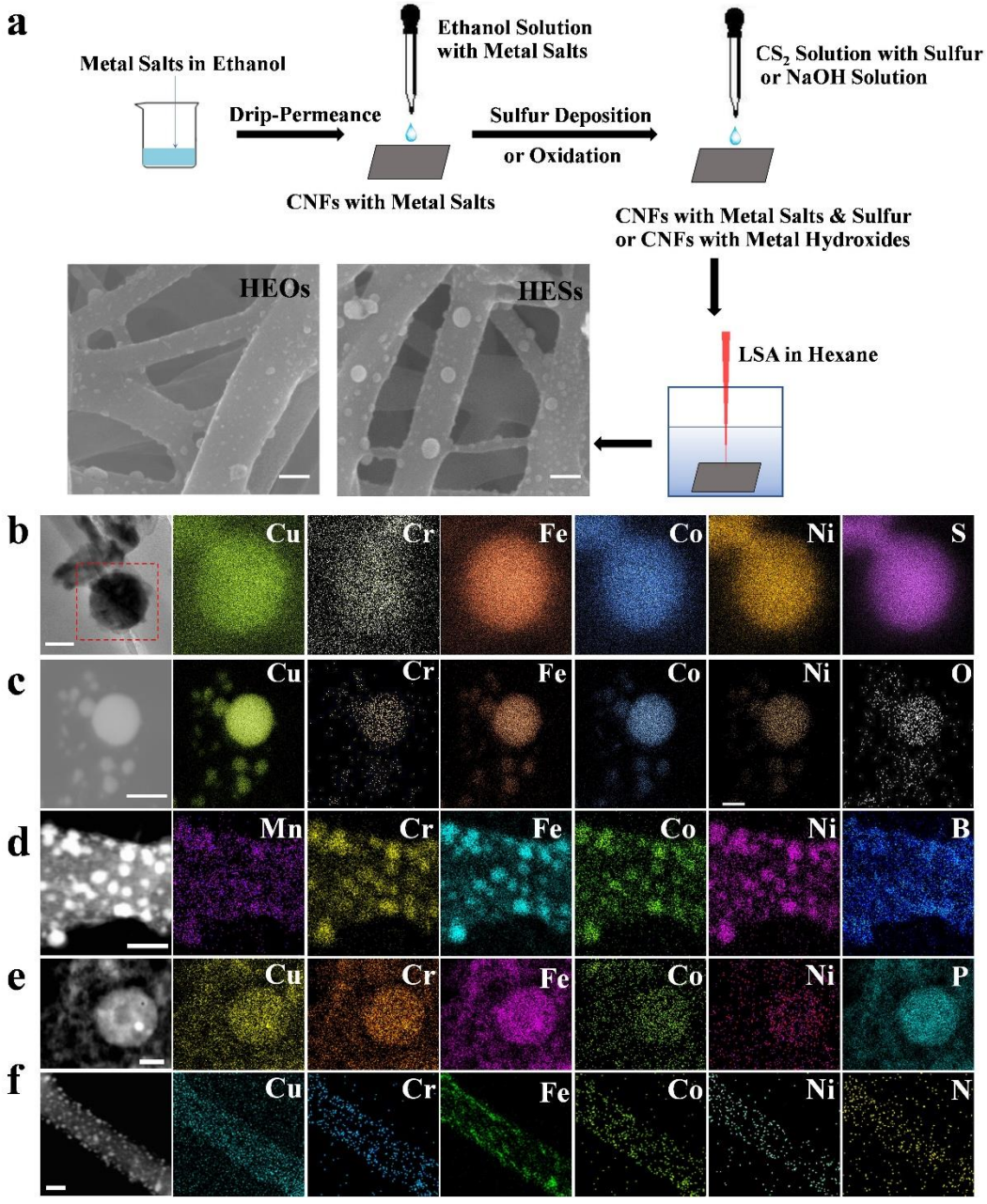


303

304 **Fig. 3. LSA synthesis of HEC NPs. a,** Schematic diagram of synthesizing HES/HEO NPs by

305 LSA, and SEM images (scale bar=100 nm) of HEOs and HESs loaded on CNFs. A TEM image

306 (scale bar=50 nm) and EDS maps of **b,** HES, **c,** HEO, **d,** HEB, **e,** HEP and **f,** HEN NPs loaded

307 on CNFs.

308

309

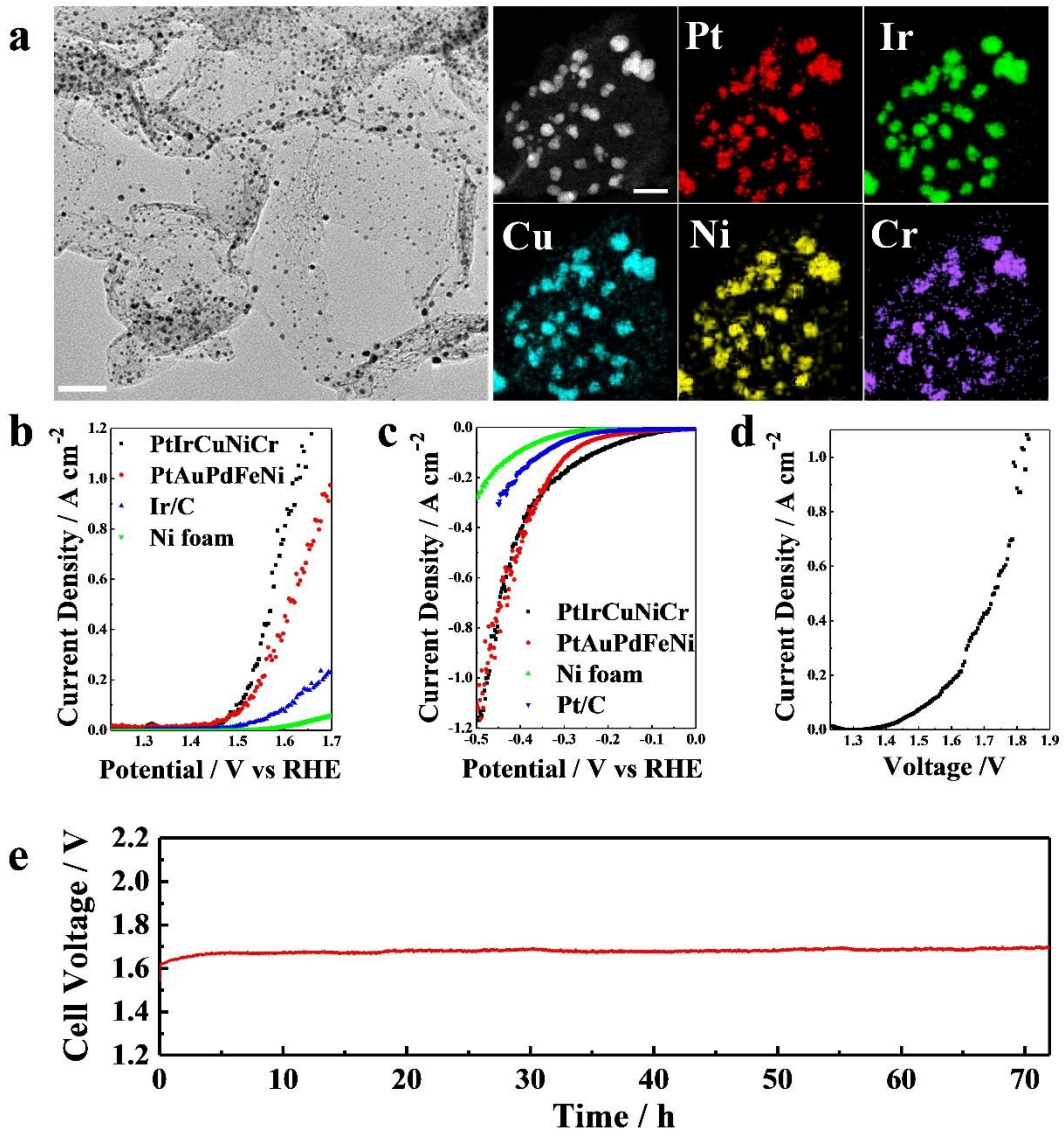


310

311 **Fig. 4. Electrocatalytic performance of HEM NPs for water splitting. a,** A TEM image

312 (scale bar= 50 nm), a HAADF image (scale bar=10 nm) and STEM elemental maps of

313 PtIrCuNiCr loaded on graphene. LSV curves of **b,** OER and **c,** HER for electrocatalysts of

314 PtIrCuNiCr, PtAuPdFeNi, Ir/C and Ni foam. **d,** An LSV curve of two-electrode cell assembled

315 by bifunctional PtIrCuNiCr-graphene electrocatalysts as both cathode and anode. **e,** Durability

316 test of the two-electrode cell at 200 mA $cm^{-2}$.

317

## Methods

### M1. Synthesis of Carbon Nanofibers

The electrospinning solution was prepared by dissolving 0.8 g electrospun polyacrylonitrile (PAN) fibers (purchased from Macklin) in 10 mL DMF at 80 °C for 12 h in a water bath to form a homogenous solution. The precursor solution was transferred to a syringe before electrospinning at a voltage of 15 kV, a spinning distance of 10 cm, and a feed rate of 0.25 mL/hour. The electrospun fibers were collected on a drum. The PAN nanofibers were first stabilized at 533K for 5 hours in air and then carbonized at 1073 K for 2 hours in nitrogen.

### M2. Synthesis of Graphene

Typically, 4 mmol D-glucose, 6 mmol $NH_4Cl$ and 80 g metal chloride salts (KCl/NaCl = 51/49 by weight) were thoroughly mixed by ball-milling treatment, followed by drying at 150 ºC for 8 h. Then the pre-reacted brown mixture was transferred to a porcelain crucible and pyrolyzed at 1050 ºC under $N_2$ for 1 h with the heating rate of 35 ºC/min. After natural cooling to ambient temperature, the blacked products were thoroughly ultrasonically rinsed with distilled water and ethanol for around several times.

### M3. Precursor-loading on Substrates

Various chloride salts were mixed in ethanol with 0.01 M for each metallic element. The mixed solution was directly dropped onto the wood/glass/copper foam/CNF film with a loading of ~1 ml/cm$^2$ or onto the graphene/nanotube with a loading of ~0.1 ml/mg. Then the loaded substrates were transferred to a vacuum oven for drying at room temperature.

## M4. Synthesis of HEAs on Substrates via LSA Method

HEA nanoparticles (NPs) on the surface of substrates were prepared by pulsed laser ablation of the corresponding precursor-loaded substrates (i.e. CNFs, wood, glass and cooper foam) which were placed on the bottom of a glass vessel filled with alkanes (i.e. hexane, octane, decane, dodecane). Hexane was used because it can maintain the precursors on substrates before LSA process due to their immiscibility, and the oxygen-free structure is beneficial to keep the as-prepared HEA NPs from being oxidized. It is important to note that the liquid phase environment in LSA is more favorable to reduce the element loss caused by vapor pressure than the gas phase environment. The substrates were kept at 10 mm under the surface of the alkanes, and was scanned by pulse laser for several cycles.

For the substrates of graphene and nanotube with the state of powder, we firstly dispersed precursors-loaded the substrates in hexane with 0.5 mg/ml by magnetic stirring. Then the solution was irradiated under agitation with the fiber laser for 30 min, ensuring all the substrates can interact with the laser beam.

## M5. Synthesis of HECs on Substrates via LSA Method

For synthesizing high entropy sulfides (HESs), the salt precursor-loaded substrates were dipped into $CS_2$ solution with sulfur of 0.1 M to allow a uniform sulfur layer deposited on the surface of the substrate before the laser irradiation. Then the substrates were transferred into hexane for laser irradiation. The laser parameters used are the same as that in the preparation of HEA NPs.

For synthesizing high entropy oxides (HEOs), the salt precursor-loaded substrates were treated by NaOH solution of 0.1 M to change the metal salt chlorides into metal oxides on the surface of the substrate before the laser irradiation. Then the substrates were transferred into hexane for laser irradiation. The laser parameters used are the same as that in the preparation of HEA NPs.

For synthesizing high entropy borides (HEBs), phosphides (HEPs) and nitrides (HENs), the salt precursor-loaded substrates were dipped into sodium borohydride, phosphoric acid and ammonium chloride aqueous solution of 0.1 M, respectively, before the laser irradiation. Then the substrates were transferred into hexane for laser irradiation. The laser parameters used are the same as that in the preparation of HEA NPs.

**M6. Electrocatalytic Experiments for Water Splitting**

The as-prepared HEA NPs on graphene as well as Pt/C and Ir/C samples were prepared by ultrasonically mixing 10 mg of the catalyst powder with the mixture of 400 μL ethanol, and 50 μL 5% Nafion solution for 20 min to form homogeneous inks. For the preparation of the catalytic electrodes, 200 μL of the ink was carefully dropped onto a nickle foam (NF, 0.5×0.5 $cm^2$) resulting in a HEA NPs/graphene loading of 18 mg $cm^{-2}$. Based on the results of inductively coupled plasma mass spectroscopy (ICP-MS), the actual HEA NPs loading was about 0.7 mg $cm^{-2}$. The electrocatalytic electrode was dried at room temperature naturally.

Electrocatalytic experiments were performed on a CHI 660D electrochemical analyzer (CH Instruments, Inc., Shanghai) with a three-electrode cell system for $O_2$ evolution reaction (OER) and $H_2$ evolution reaction (HER). The catalyst ink-loaded NF was used as the working

electrode, a Ag/AgCl (sat. KCl) electrode as the reference electrode, and a carbon rod as the counter electrode. All the electrochemical experiments were conducted in a 1.0 M KOH aqueous solution at room temperature. All potentials for OER and HER reported herein were referenced to the reversible hydrogen electrode (RHE).

The overall water splitting was performed in a two-electrode system with 1.0 m KOH electrolyte, in which one PtIrCuNiCr-NF served as the negative electrode for HER and another one acted as the positive electrode for OER. The durability was assessed at an applied potential to reach a catalytic current density of 200 mA $cm^{-2}$ for 72 h.

**M7. Characterizations**

The morphology of as-prepared samples was examined by the field emission scanning electron microscopy (FE-SEM, FEI NOVA NanoSEM230, USA) and transmission electron microscopy (TEM, JEOL 3010, Japan). An energy-dispersive X-ray spectroscopy (EDS, Oxford instruments X-Max) equipping on the FE-SEM was used to obtain the element distribution of HEAs on the wood or nickle foam. An EDS (Elite T EDS System) equipping on the TEM was employed to record the element distribution of HEAs on graphene, CNTs and CNFs. HAADFSTEM analysis is characterized using a JEM Titan G2 60-300 TEM (JEOL) with 60-300 kV. To prepare the TEM and STEM specimen, the synthesized samples were dispersed in ethanol by ultrasonic treatment, and then transferred onto micro grids. In this process, it is inevitable to separate some HEA nanoparticles from substrates. The crystal structures of the samples were measured by a powder X-ray diffractometer (XRD, Ultima III, Rigaku Corp., Japan) using Cu-Kα radiation (λ = 1.54178 Å, 40 kV, 40 mA). The atomic ratios

of HEM NPs were analyzed by PerkinElmer AVIO500 ICP-MS. The solutions were prepared by digesting the samples in aqua regia followed by dilution with 2% hydrochloric acid. The surface composition of the samples was performed by X-ray photoelectron spectroscopy (XPS, ESCALAB 250) with the non-monochromatic Al Kα X-ray as the X-ray source. The binding energy of C1s (284.6 eV) was used to calibrate the other binding energies. UV-vis diffuse reflectance spectroscopy (UV–vis-DRS) was measured on a PerkinElmer Lambda 950 UV/Vis/NIR spectrometer.

**Acknowledgments** This work was supported by the National Key Research and Development Program of China (2018YFE0208500), the Major Research Plan of the National Natural Science Foundation of China (91963206), the National Natural Science Foundation of China (52072169, 51627810, 51972164), the Natural Science Foundation of Jiangsu Province (BK20201202), the Program for Guangdong Introducing Innovative and Enterpreneurial Teams (2019ZT08L101), the Open Fund of Wuhan National Laboratory for Optoelectronics (2018WNLOKF020), Postgraduate Research & Practice Innovation Program of Jiangsu Province (KYCX19_0043), the Fundamental Research Funds for the Central Universities (14380180), and Civil Aerospace Technology Research Project (B0108).

**Author contributions:** B. Wang, Y. Yao, Z. Lin and Z. Zou conceived the idea and designed the present work. B. Wang carried out the experiments. C. Wang, X. Yu and C. Wu performed detailed microscopic characterizations. Y. Cao, L. Gao and W. Luo directed the catalytic evaluation.

**Competing interests:** The authors declare no competing interests. Provisional patent applications have been applied through Nanjing University (202011094113.4 and 20254CJH)

**Additional information:** Supplementary information is available for this paper. Correspondence and requests for materials should be addressed to Z. Z., Z. L. or Y. Y.

## Extended Data

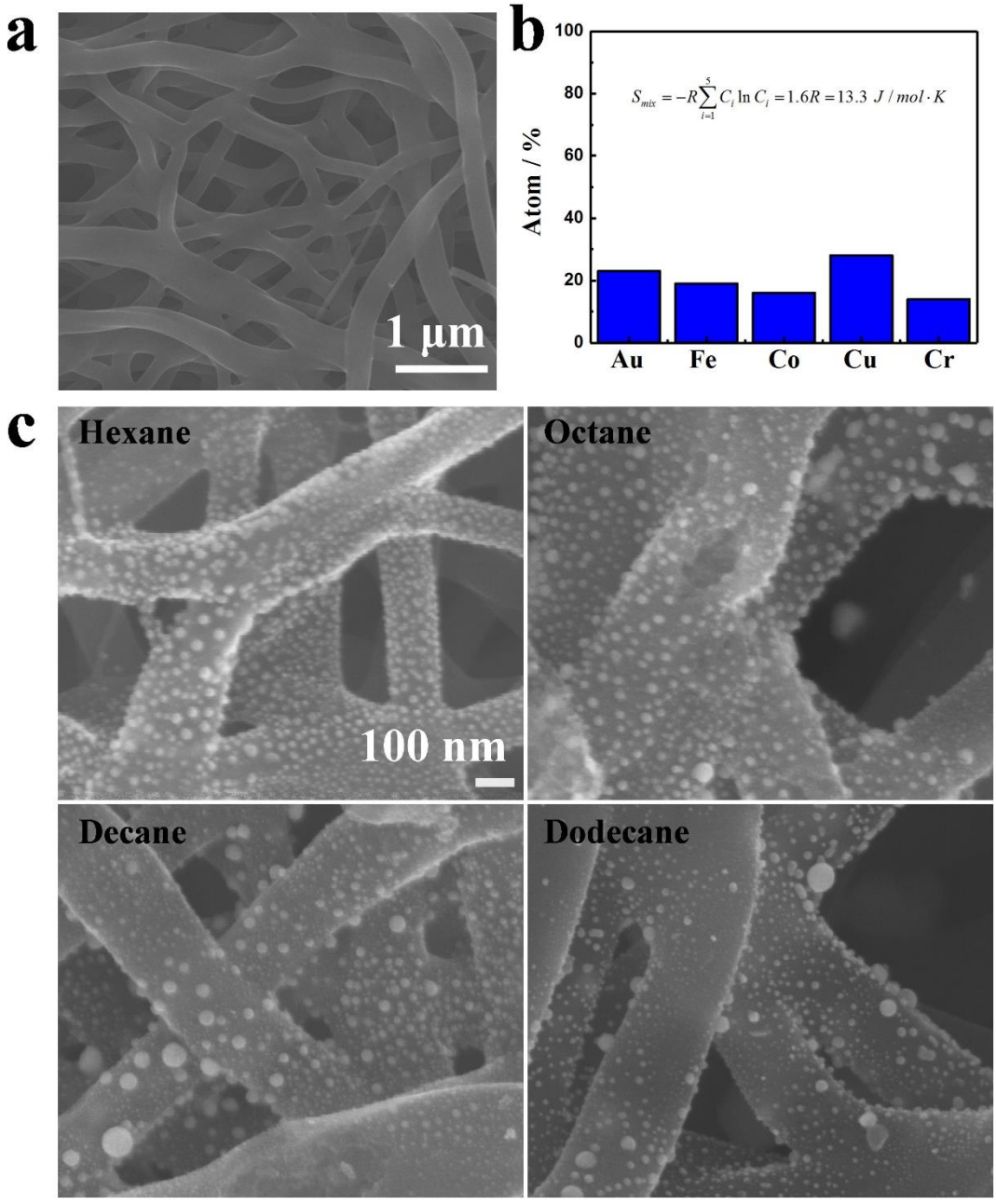


**Extended Data 1 Liquid phase applicability of the LSA method. a,** An SEM image of the as-prepared CNFs. **b,** Atomic percentages of quinary HEA NPs (AuFeCoCuCr). **c,** SEM images of PtAuCuFeCo HEA NPs synthesized in hexane, octane, decane and dodecane, respectively, during LSA process.

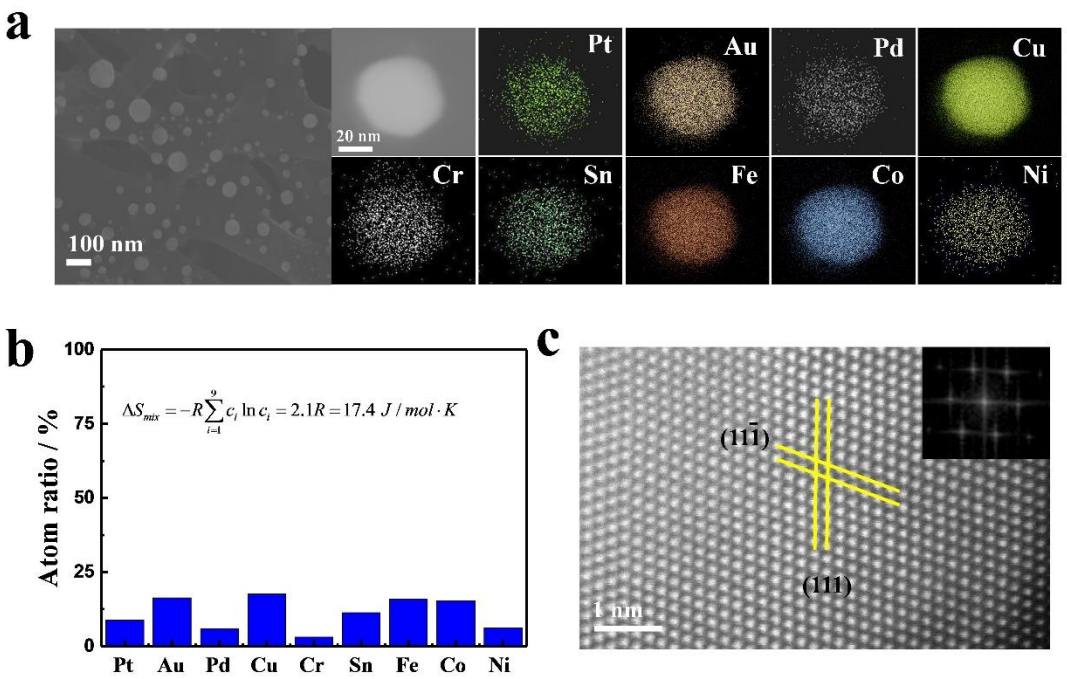


**Extended Data 2 Novenary HEA NPs synthesized by the LSA method. a,** An SEM image of PtAuPdCuCrSnFeCoNi HEA NPs loaded onto CNFs. A TEM image and the EDS maps of Pt, Au, Pd, Cu, Cr, Sn, Fe, Co, Ni elements of the novenary HEA NPs. **b,** Atomic percentages of the novenary HEA NPs. **c,** A HAADF-STEM image with Fourier transform analysis.

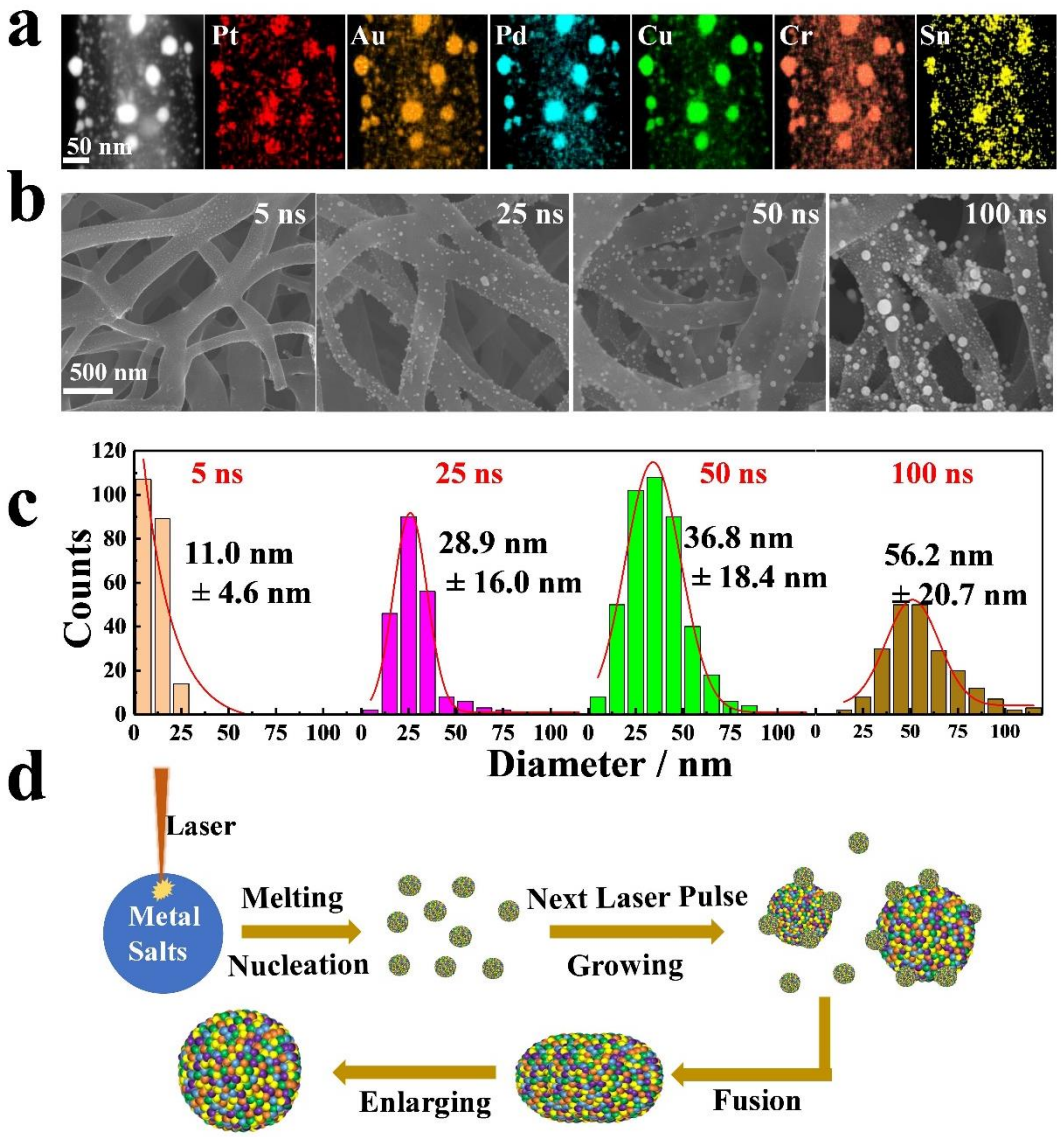


436

437 **Extended Data 3 Size control of HEA NPs *via* laser scanning cycles. a,** EDS maps of Pt, Au,

438 Pd, Cu, Cr, Sn elements in the HEA NPs loaded on CNFs with laser scanning cycles of 20

439 times. **b,** SEM micrographs and **c,** the corresponding size distributions of the PtAuPdCuCrSn

440 NPs under different laser interaction time. **d,** Schematic diagram of HEA NP formation and

441 enlarging under repeated laser pulse.

442

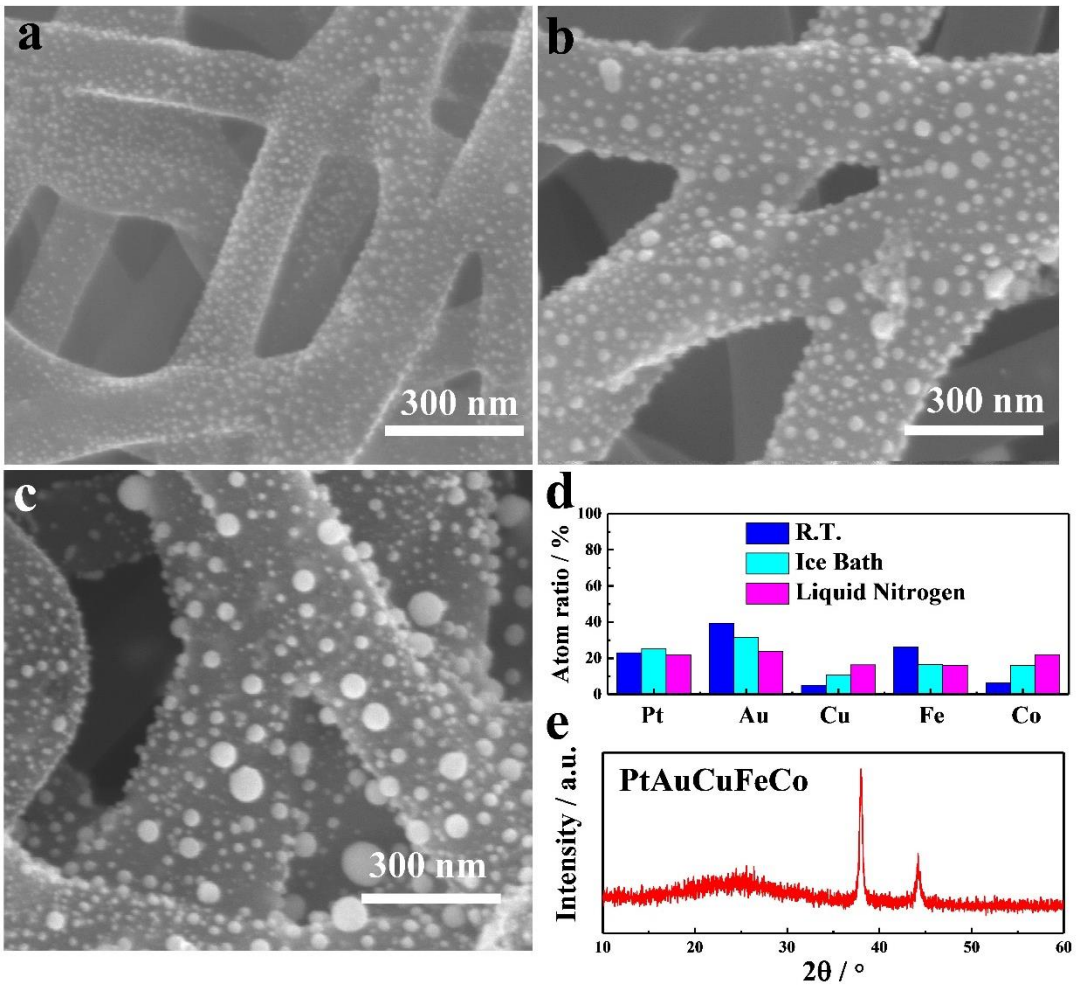


**Extended Data 4 Size control of HEA NPs *via* liquid phase temperature.** SEM images of HEA NPs of PtAuCuFeCo synthesized at **a,** -196, **b,** 0 and **c,** 25 °C, respectively. **d,** Atom ratios of Pt, Au, Cu, Fe, Co in HEA NPs prepared under room temperature (R.T.), ice bath and liquid nitrogen, respectively. **e,** XRD profile of HEA NPs of PtAuCuFeCo synthesized at -196 °C.

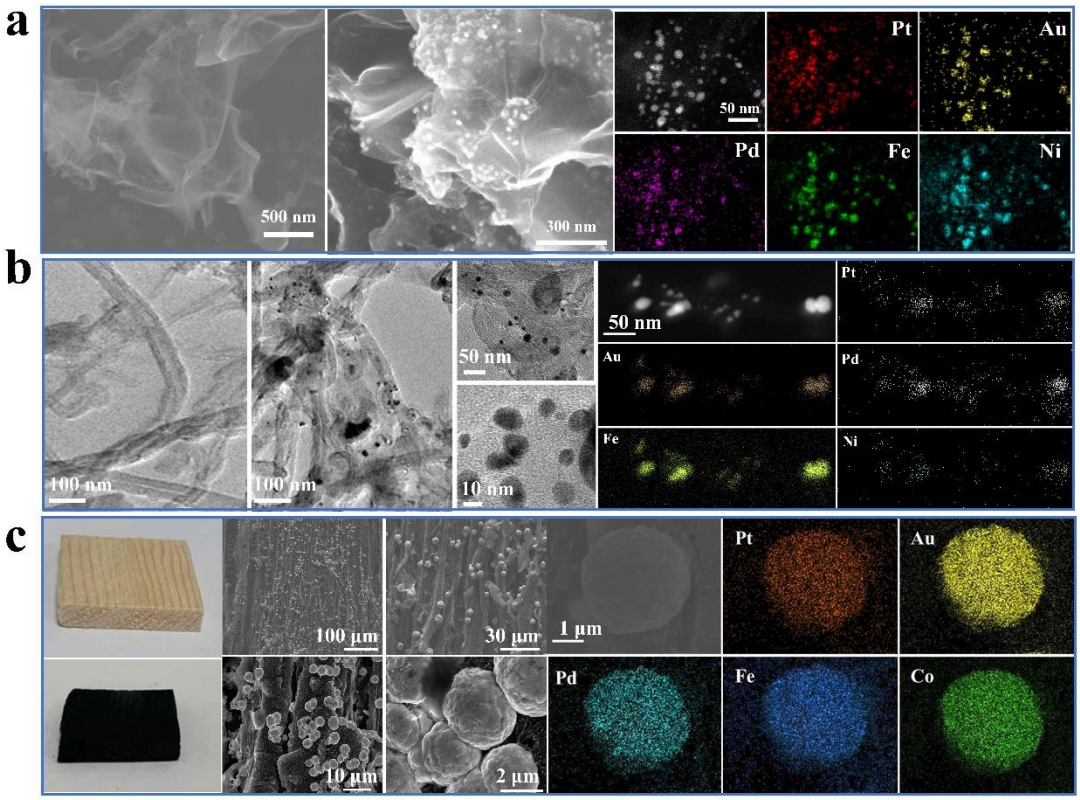


**Extended Data 5 Nanoparticles immobilized on different carbon substrates. a,** SEM images of as-prepared graphene, graphene with HEA NPs (PtAuPdFeNi) as well as its HAADF image and the STEM elementary maps. **b,** TEM images of pristine CNTs, CNTs with PtAuPdFeNi HEA NPs at different magnifications as well as the EDS maps. **c,** Photographs of a piece of wood before and after carbonization. SEM images of HEA NPs (PtAuPdFeCo) on carbonized wood at different magnifications as well as the EDS maps.

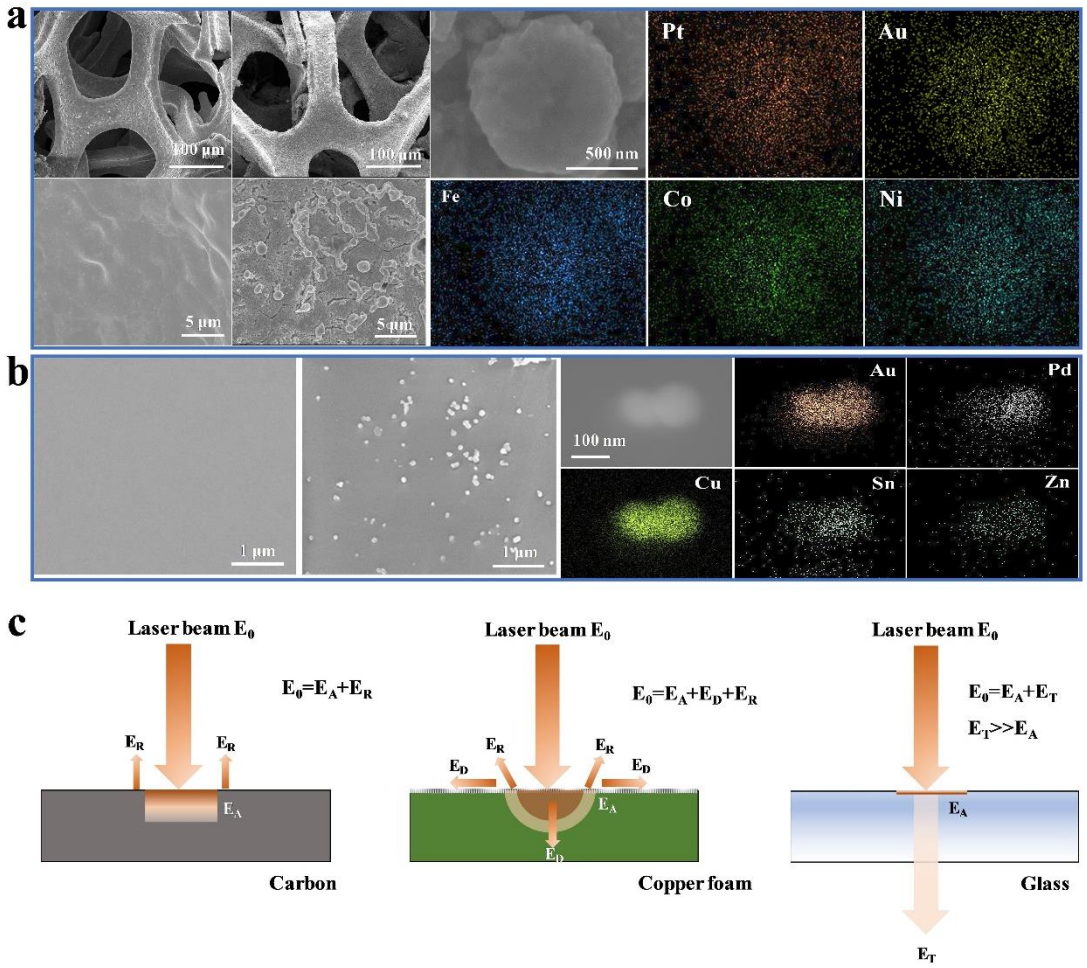


457

458 **Extended Data 6 Nanoparticles immobilized on substrates other than carbon. a,** The SEM
459 images of a pristine Cu foam and the PtAuFeCoNi HEA NPs-loaded Cu foam at low and high
460 magnification; SEM images and elementary maps of HEA NPs-loaded on Cu foam. **b,** SEM
461 images of a pristine glass slide and HEA NPs (AuPdCuSnZn)-loaded glass slide; A TEM image
462 and the EDS maps of the HEA NPs-loaded glass slide. **c,** Representation of energy
463 redistribution for different substrates under laser pulse. $E_R$: reflected energy, $E_T$: transmitted
464 energy, $E_A$: absorbed energy, $E_D$: diffused energy.

465

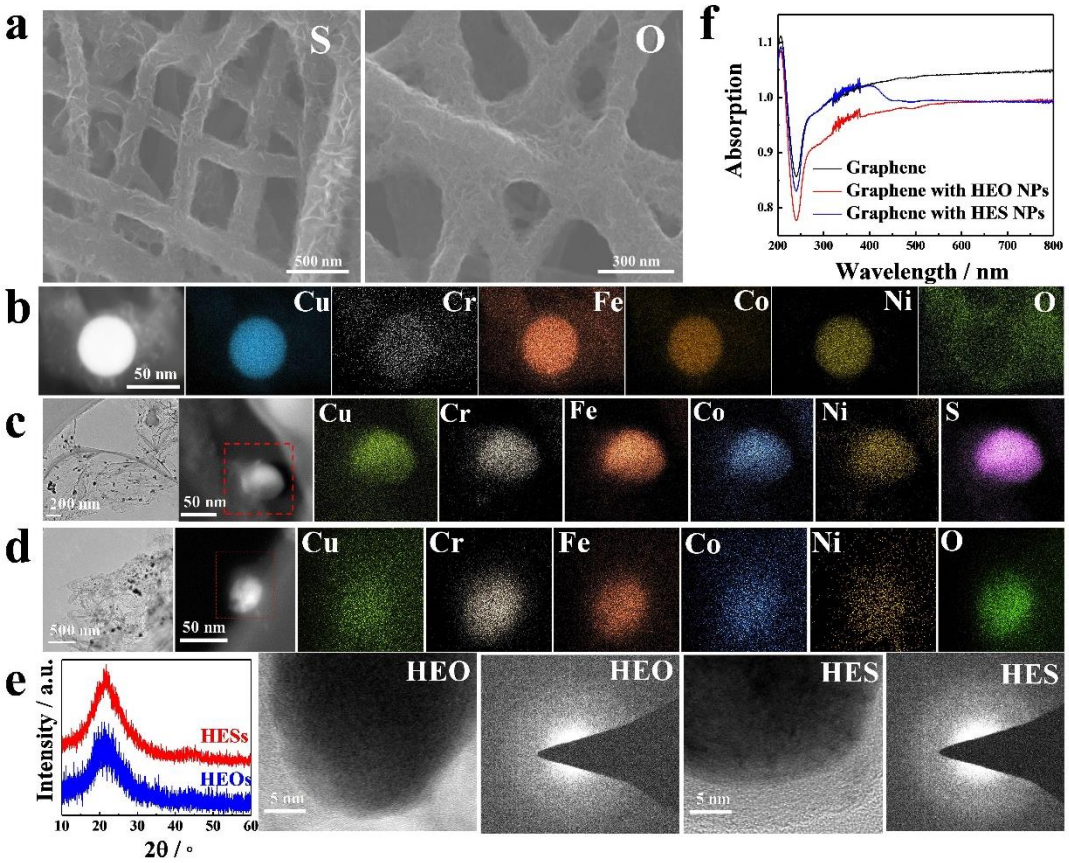


466

467 **Extended Data 7 HEO and HES NPs on carbon substrates. a,** SEM images of CNFs loaded
468 with precursors of sulfur, $CuCl_2$, $CrCl_3$, $FeCl_3$, $CoCl_2$, $NiCl_2$ and precursors of $CuCl_2$, $CrCl_3$,
469 $FeCl_3$, $CoCl_2$, $NiCl_2$ treated by NaOH solution, respectively. **b,** A TEM image and the EDS
470 maps of CuCrFeCoNi NPs. **c,** TEM and HRTEM images of CuCrFeCoNiS NPs on graphene
471 and their EDS maps. **d,** TEM and HRTEM images of CuCrFeCoNiO NPs on graphene and
472 their EDS maps. **e,** XRD patterns of graphene loaded with HEOs and HESs; HRTEM images
473 coupled with SAED patterns of HEOs and HESs. **f,** The UV-vis spectra of pristine graphene,
474 graphene with the HEO and HES NPs, respectively.

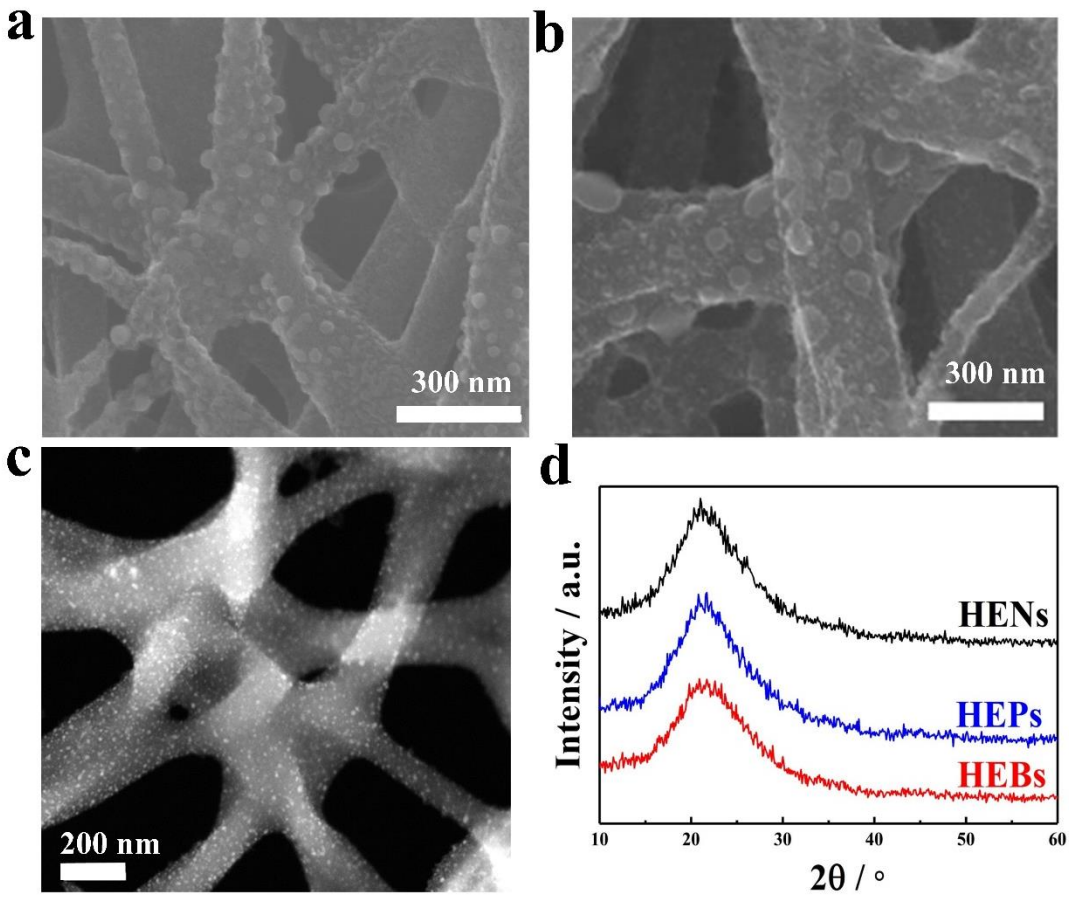


475

476 **Extended Data 8 HEB, HEP and HEN NPs on CNFs.** SEM images of HEC NPs with the

477 elements of **a,** Cr, Fe, Co, Ni, Mn, B, **b,** Cu, Cr, Fe, Co, Ni, P on CNFs, respectively. **c,** A TEM

478 image of HEC NPs with the elements of Cu, Cr, Fe, Co, Ni, N on CNFs. **d,** XRD patterns of

479 CNFs loading with the HEBs, HEPs, and HENs NPs.

480

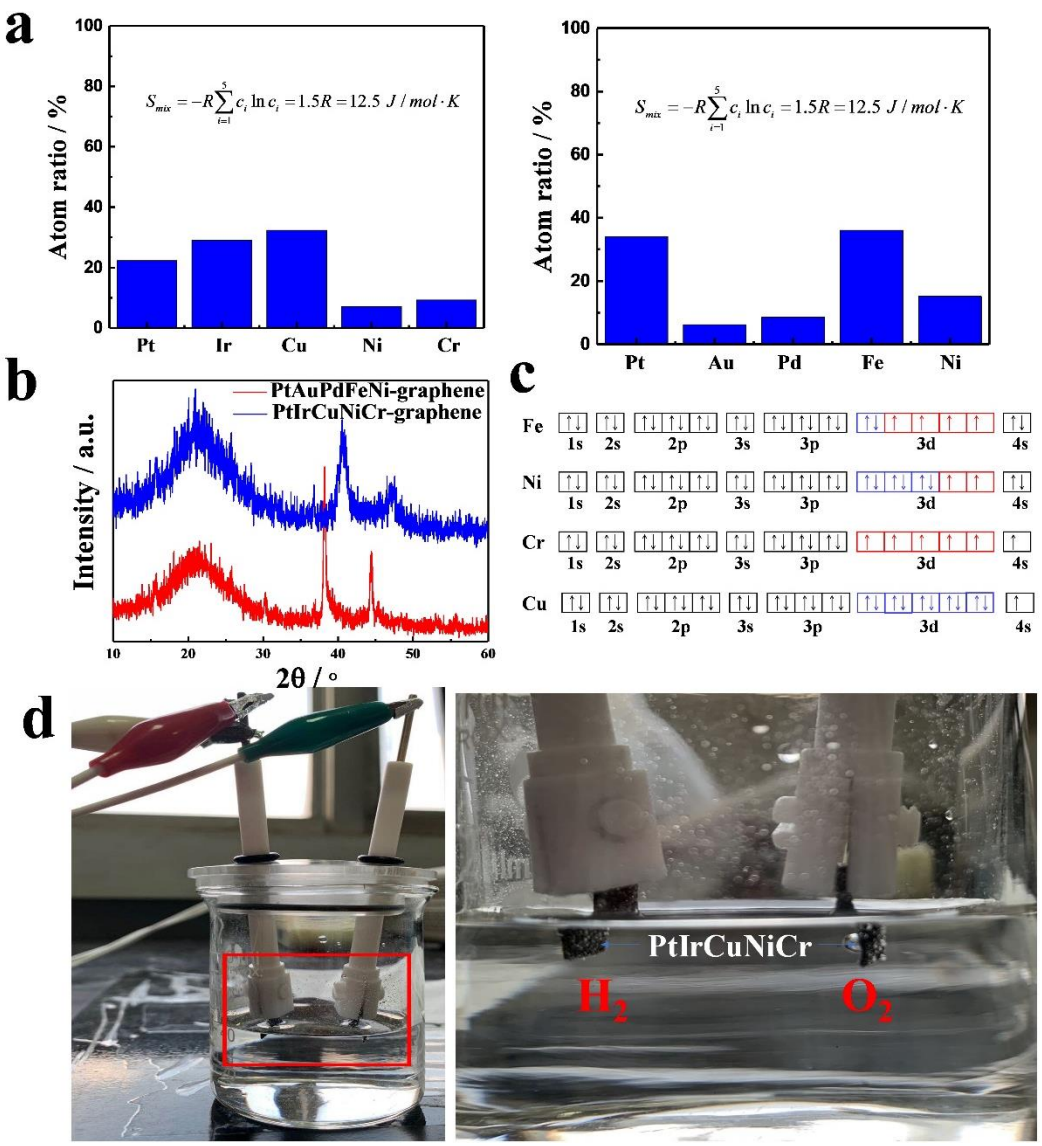


**Extended Data 9 Water splitting using HEA NPs as electrocatalysts. a,** Atomic ratios of PtIrCuNiCr and PtAuPdFeNi NPs on graphene, respectively. **b,** The XRD patterns of PtIrCuNiCr and PtAuPdFeNi NPs on graphene. Simple solid solution phase with FCC crystalline structure form. The angular deviation of the diffraction peaks between these two samples is caused by different levels of lattice distortions. **c,** Electron configuration diagrams of Fe, Ni, Cr, Cu elements. **d,** Photographs of electrolytic cell for overall water splitting with PtIrCuCrNi NPs as a bifunctional electrocatalyst (entire setup and close-up of the red box region).

# Figures

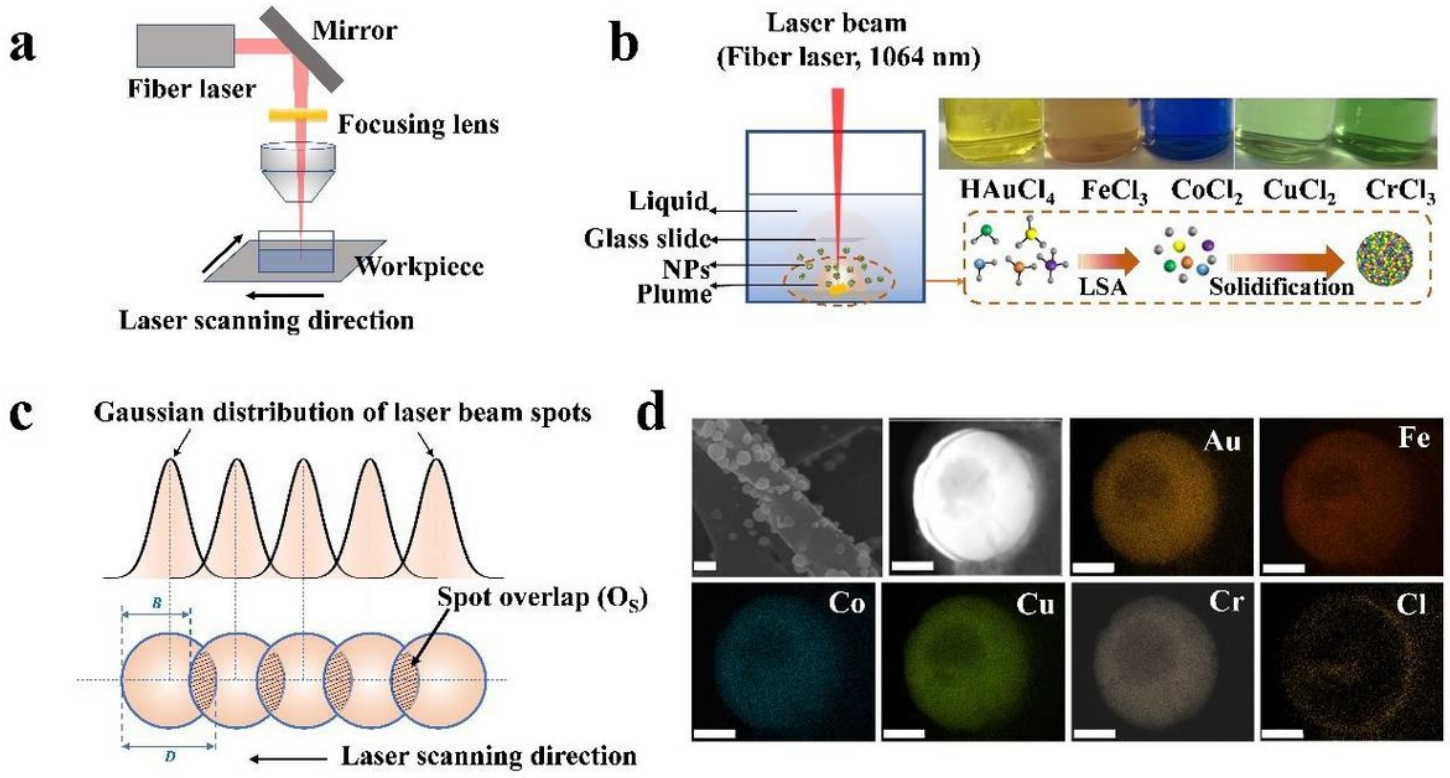


Figure 1

LSA synthesis of HEA NPs. The schematic diagram of a, experimental set-up and b, reaction process for synthesizing AuFeCoCuCr HEA NPs by the LSA method. c, The energy distribution of a Gaussian laser beam with the power density of 2×109 W/cm2 for the pulsed fiber nanosecond laser. d, An SEM image of AuFeCoCuCr HEA NPs loaded on CNFs with the scale bar of 100 nm; a TEM image of a AuFeCoCuCr HEA NP with the scale bar of 20 nm and the corresponding EDS maps of Au, Fe, Co, Cu, Cr, Cl elements.

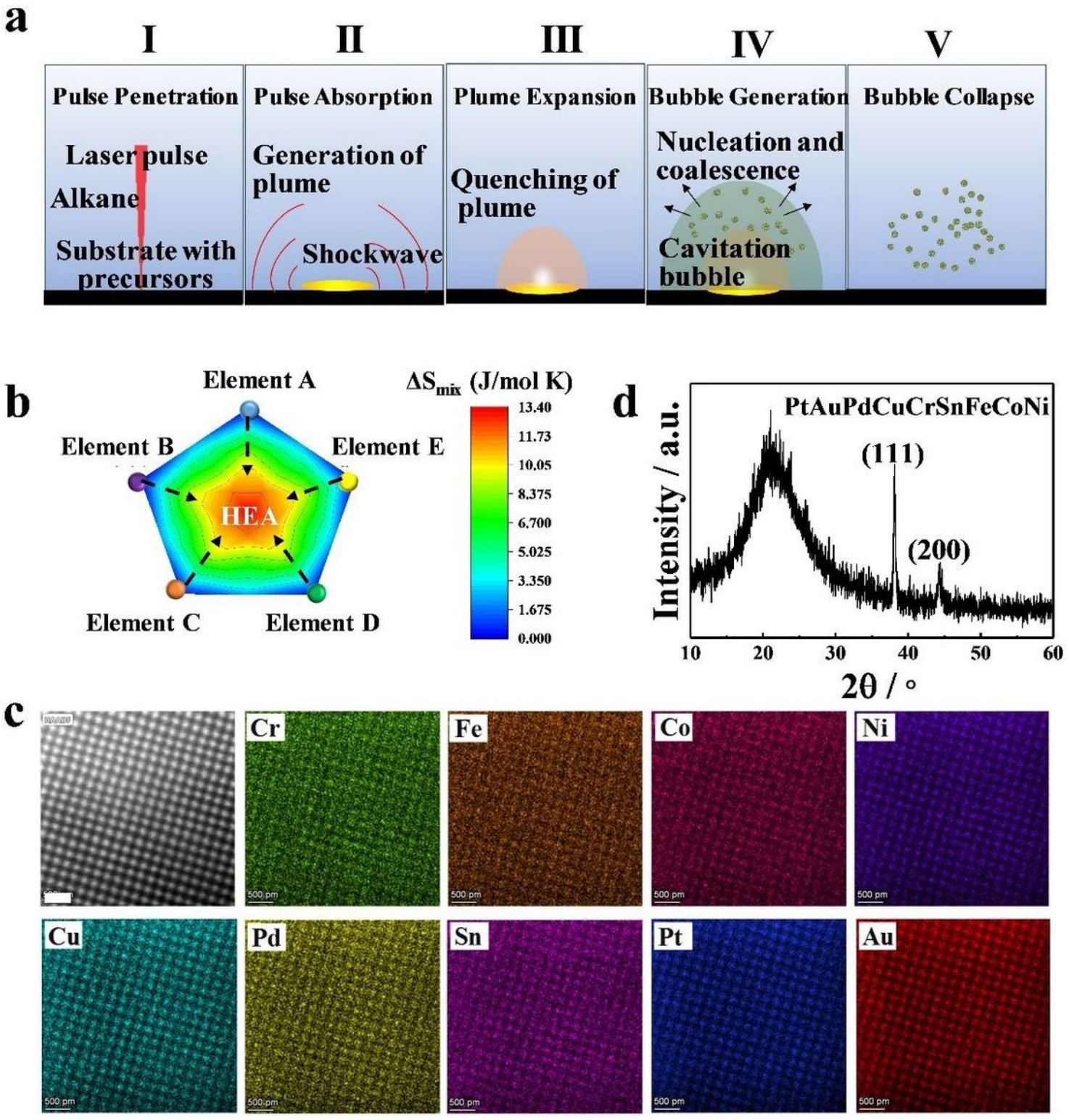


## Figure 2

Formation mechanisms of HEA NPs for the LSA strategy. a, Schematic illustration of formation mechanism of HEA NPs by LSA method. b, The configurational entropy evolution of HEAs with five elements during LSA process. c, Comparison of the local concentration distribution of individual elements for the same region. Atomic-scale HAADF-STEM images and STEM elemental maps for a novenary HEA NP (PtAuPdCuCrSnFeCoNi). d, XRD pattern of the novenary HEA-NPs.

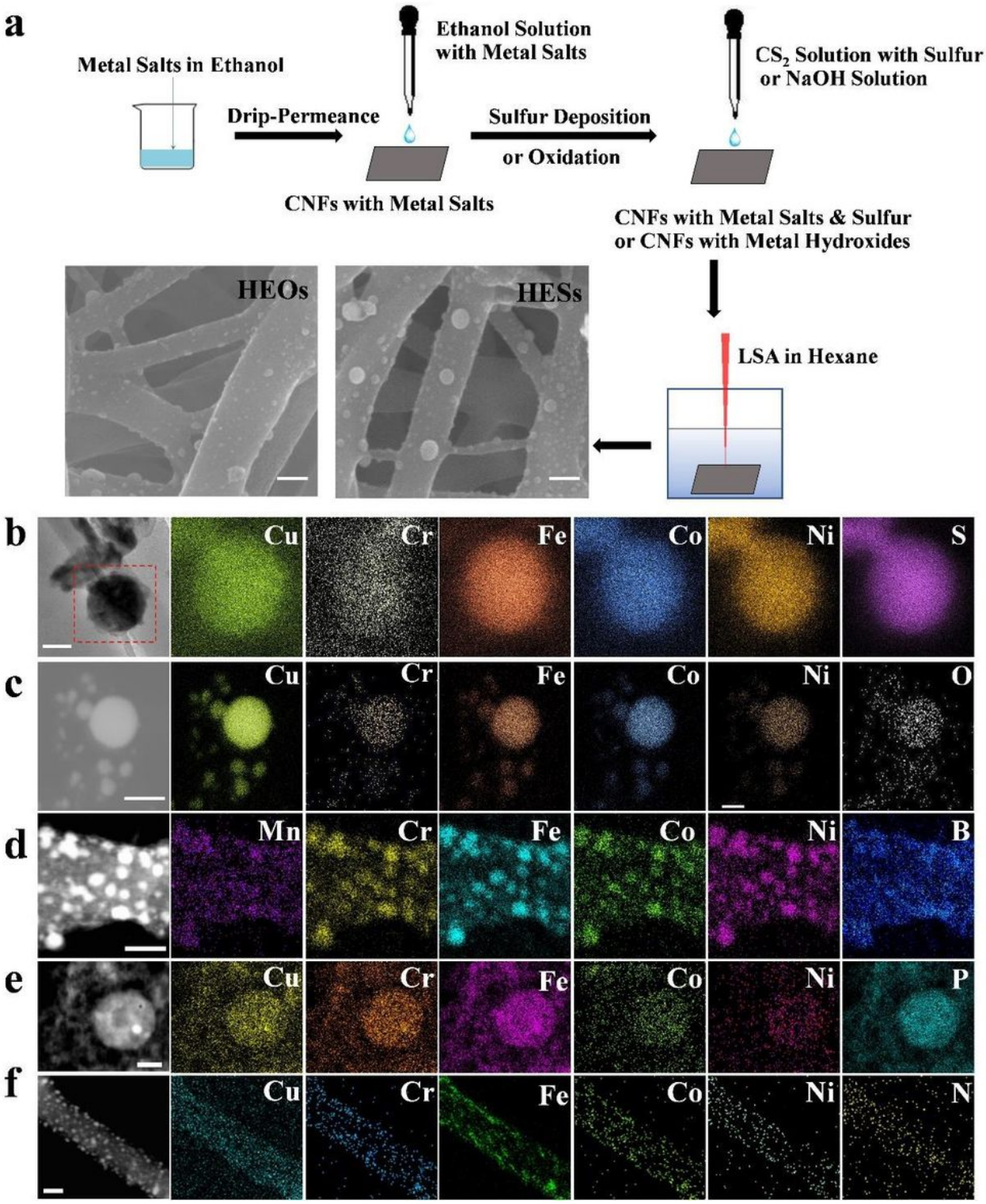


## Figure 3

LSA synthesis of HEC NPs. a, Schematic diagram of synthesizing HES/HEO NPs by LSA, and SEM images (scale bar=100 nm) of HEOs and HESs loaded on CNFs. A TEM image (scale bar=50 nm) and EDS maps of b, HES, c, HEO, d, HEB, e, HEP and f, HEN NPs loaded on CNFs.

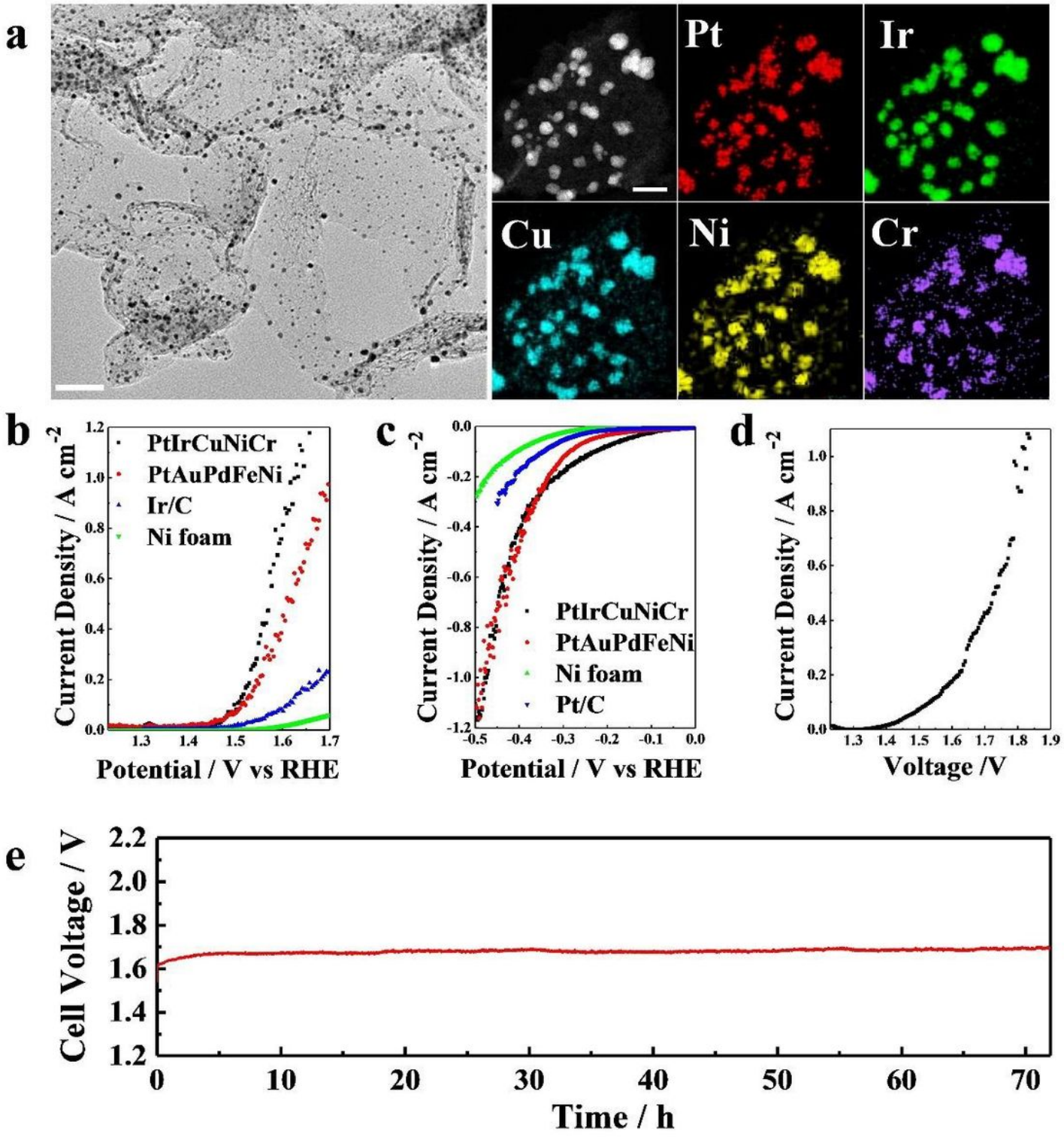


Figure 4

Electrocatalytic performance of HEM NPs for water splitting. a, A TEM image (scale bar= 50 nm), a HAADF image (scale bar=10 nm) and STEM elemental maps of PtIrCuNiCr loaded on graphene. LSV curves of b, OER and c, HER for electrocatalysts of PtIrCuNiCr, PtAuPdFeNi, Ir/C and Ni foam. d, An LSV curve of two-electrode cell assembled by bifunctional PtIrCuNiCr-graphene electrocatalysts as both cathode and anode. e, Durability test of the two-electrode cell at 200 mA cm-2.

# Supplementary Files

This is a list of supplementary files associated with this preprint. Click to download.

- MovieS1.mp4
- Supplementaryfile.pdf